

Article

Multi-Channel Sensing System Utilizing Mott Memristors for Single-Wire Data Fusion and Back-End Greedy Strategy Data Recovery

Shiquan Fan ^{1,*} , Peihao Liu ¹, Yongqiang Shi ¹, Shujing Zhao ¹, Chuanyu Han ¹, Junyi Xu ² and Guohe Zhang ^{1,*}

¹ School of Microelectronics, Xi'an Jiaotong University, Xi'an 710049, China; l371122ph@stu.xjtu.edu.cn (P.L.); syq506912088@stu.xjtu.edu.cn (Y.S.); zhaoshujing@stu.xjtu.edu.cn (S.Z.); hanchuanyu@xjtu.edu.cn (C.H.)

² Aerial Photogrammetry and Remote Sensing Group Co., Ltd. of CNACG (ARSC), Xi'an 710199, China; junyixu_lm@163.com

* Correspondence: junjunfan@xjtu.edu.cn (S.F.); zhangguohe@xjtu.edu.cn (G.Z.)

Abstract: This paper presents a novel Mott memristor-based multi-channel sensing system designed for the simultaneous processing of multiple sensing channels, employing single-wire data fusion and a greedy search strategy for back-end data recovery. Multiple channels of external stimulus information are simultaneously encoded into analog signals with varying frequencies, utilizing a Mott memristor array. Auxiliary circuits then convert the analog sensing signals into square wave signals which are further transformed into narrow (100 ns) pulse signals through pulse generation circuitry. Subsequently, these narrow pulse signals are fused into a single-wire signal by using an OR gate. At the back-end of the system, a greedy searching strategy is applied to accurately identify all frequencies within the fused pulse signal, enabling seamless analog-to-frequency conversion across multiple channels. The system is suitable for a wide range of sensors and can be directly connected to FPGAs for data processing, eliminating the need for traditional analogue front-end and ADC circuits and greatly reducing circuit complexity and power consumption. By leveraging the innovative capabilities of Mott memristors, the proposed system achieves precise analog-to-frequency conversion with significantly reduced power consumption.

Keywords: mott memristor; multi-channel sensing system; single-wire signal; greedy search strategy



Citation: Fan, S.; Liu, P.; Shi, Y.; Zhao, S.; Han, C.; Xu, J.; Zhang, G. Multi-Channel Sensing System Utilizing Mott Memristors for Single-Wire Data Fusion and Back-End Greedy Strategy Data Recovery. *Electronics* **2024**, *13*, 345. <https://doi.org/10.3390/electronics13020345>

Academic Editor: Masum Hossain

Received: 26 November 2023

Revised: 2 January 2024

Accepted: 11 January 2024

Published: 13 January 2024



Copyright: © 2024 by the authors. Licensee MDPI, Basel, Switzerland. This article is an open access article distributed under the terms and conditions of the Creative Commons Attribution (CC BY) license (<https://creativecommons.org/licenses/by/4.0/>).

1. Introduction

In recent years, there has been a growing demand for high-performance, low-power sensing systems capable of efficiently converting analog signals from multiple sensors into a digital format for further processing [1–5]. Traditional approaches often rely on complex analog front-end circuits and analog-to-digital converters (ADCs), which not only consume significant power but also introduce design complexities. To address these challenges, researchers have been exploring alternative solutions that offer improved efficiency and reduced power consumption [6–10]. One such innovative solution is the integration of Mott memristors into multi-channel sensing systems [11]. Mott memristors, with their unique characteristics such as non-volatile resistance switching behavior and low power consumption, have emerged as promising devices for analog signal processing. They enable multi-channel analog-to-frequency conversion, making them ideal for applications with a large number of sensors.

This work introduces a novel approach that leverages a Mott memristor array integrated with auxiliary circuits to convert analog signals into square wave signals with varying frequencies. The square wave signals are then transformed into pulse signals through dedicated pulse generation circuitry and integrated using an OR gate to achieve data fusion. At the backend of the system, a greedy search algorithm accurately identifies all frequencies present in the fused pulse signal, enabling multi-channel analog-to-frequency conversion.

Compared to traditional approaches, the Mott memristor-based multi-channel sensing system offers several advantages [12–17]. Firstly, it significantly reduces power consumption while simplifying circuit design. By leveraging Mott memristors for efficient analog-to-frequency conversion, the system eliminates the need for power-hungry ADCs, resulting in substantial power savings. Additionally, the seamless integration of the system with FPGA platforms enables efficient data processing, further enhancing overall system performance.

The implications of this research are wide-ranging, with potential applications in environmental monitoring, health tracking, and industrial automation, among others [16]. By providing an efficient and reliable solution for multi-channel analog-to-frequency conversion, the proposed system holds great promise for advancing sensing technologies in various domains.

Given the limitations of traditional analog front-end circuits and the increasing demand for low-power, high-performance sensing systems, this study aims to make a significant contribution to the field of integrated circuits by introducing a novel Mott memristor-based approach for multi-channel analog-to-frequency conversion. The designed system effectively addresses the limitations of traditional analog front-end circuits, offering a high-performance, low-power solution that is particularly relevant in the context of modern integrated circuit design. By seamlessly integrating Mott memristors with auxiliary circuits and advanced signal processing techniques, this research presents a comprehensive framework for efficient multi-channel analog-to-frequency conversion, potentially impacting a broad spectrum of applications.

The subsequent sections will delve into the design and implementation details of the proposed multi-channel sensing system, followed by experimental results and discussions on its performance metrics. Finally, conclusions will be drawn, highlighting the significance of this research and outlining potential avenues for future work. By shedding light on the practical aspects and demonstrating the effectiveness of the proposed approach, we aim to not only enrich the understanding of Mott memristor-based systems but also pave the way for future innovations in the field of integrated circuits and sensor technologies.

2. Sensing System Architecture

The development of the Mott memristor-based multi-channel sensing system represents a significant breakthrough in the field of electronic sensing technologies. The architecture of the proposed sensing system is illustrated in Figure 1, showcasing its unique features and operational principles.

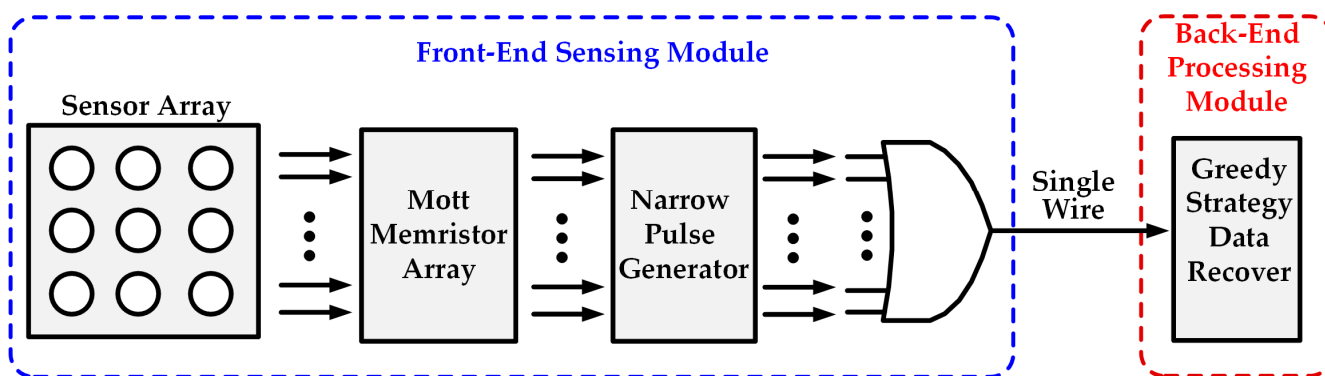


Figure 1. System architecture of the proposed Mott memristor-based multi-channel sensing system with single-wire data fusion and back-end greedy strategy data recovery.

The front-end sensing module comprises a 3×3 sensor array, a Mott memristor array, a narrow pulse generator, and an OR gate for data fusion. The sensor array is responsible for converting the external stimuli into changes in resistance and capacitance, while the Mott memristor array generates rate-coded spikes based on the changes in the sensor

array [18–21]. These spikes are then shaped into a square wave and transformed into a narrow pulse wave, which is subsequently transmitted to the FPGA board for data fusion.

To enable efficient data recovery, the single-wire output generated by the FPGA board is processed using the greedy strategy. This approach involves iteratively selecting the most significant features from the input signal, thus enabling the recovery of high-quality data with a minimal loss of information.

Overall, the proposed Mott memristor-based sensing system presents a novel and innovative approach to multi-channel electronic sensing. The combination of the sensor array and Mott memristor array facilitates the generation of rate-coded spikes, which can be efficiently processed and fused using the narrow pulse generator circuit and FPGA. The implementation of the greedy strategy for data recovery further enhances the performance and reliability of the proposed sensing system, thus establishing a solid foundation for its potential utilization across diverse electronic applications.

3. Mott Memristor

3.1. Fabrication of the Mott Memristor

The successful fabrication of the Mott memristor is essential for its potential application in electronic devices and systems. The structure of the Mott memristor is depicted in Figure 2a, while a more detailed illustration is presented in Figure 2b.

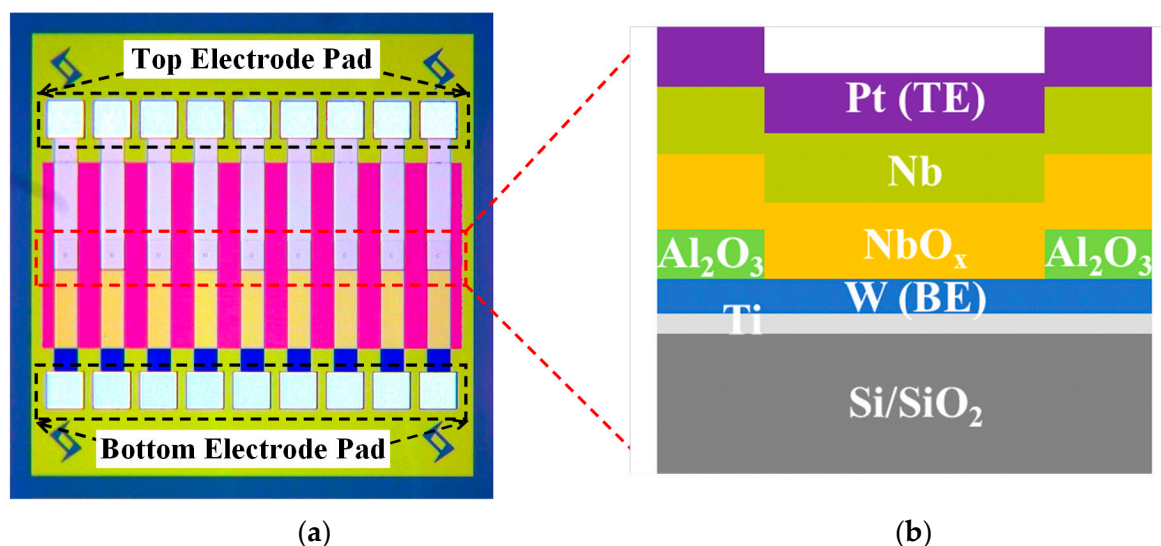


Figure 2. (a) Microscopic image of the Mott memristor array; (b) structure of the Mott memristor cell.

To fabricate the Mott memristor, a via hole ($\sim 10 \mu\text{m}$) structure of Ti/W/NbO_x/Nb/Pt crossbar is utilized on a silicon wafer with 300 nm SiO₂. The bottom electrode (BE) and insulating layer are deposited using radio frequency (RF) magnetron sputtering, with Ti/W ($\sim 10 \text{ nm}/80 \text{ nm}$) and Al₂O₃ ($\sim 30 \text{ nm}$), respectively. These layers are then patterned in a lift-off process. Subsequently, a NbO_x ($\sim 50 \text{ nm}$) film is prepared as the switching layer using RF magnetron sputtering and a Nb target in an Ar:O₂ = 30:2 sccm ambient at room temperature. Finally, the top electrode (TE) consisting of Nb/Pt ($\sim 50 \text{ nm}/100 \text{ nm}$) is sputtered and patterned [22,23].

The utilization of this specific fabrication process ensures the creation of a high-quality Mott memristor with excellent performance characteristics. The precision of the fabrication process is critical to achieving optimal device performance and reliability. Furthermore, the use of a via hole structure helps to minimize the size of the device, thus enabling its integration into small-scale electronic devices.

Overall, the successful fabrication of the Mott memristor through this specific process, together with its unique structural features, underpins its potential utilization across diverse electronic applications. Further research in this field could potentially result in the development of more advanced and efficient memristive devices.

3.2. Operating Principle of Mott Memristor

Figure 3 illustrates the current-voltage (I-V) DC sweep characteristic of the Mott memristor, showcasing its ability to undergo stable bidirectional transitions between low and high resistance states. As the applied voltage progressively increases from zero to approximately 1.57 V, a notable surge in current is observed, signifying a transition from the high-resistance state to the low-resistance state. This particular voltage level is commonly referred to as the threshold voltage (V_{th}). Conversely, when the voltage declines from 2 V to around 1.17 V, a sharp decline in current occurs, indicating a transition from the low-resistance state back to the high-resistance state. This specific voltage value is known as the hold voltage (V_{hold}).

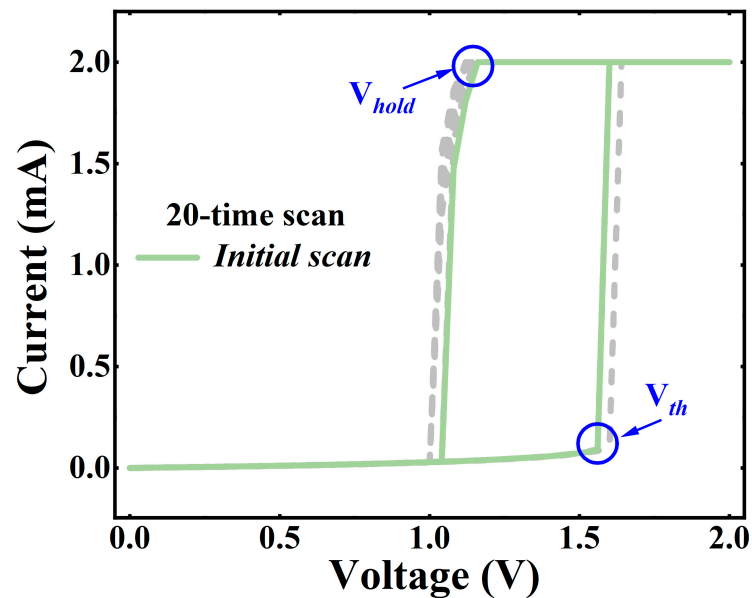


Figure 3. I-V DC sweeps of the Mott memristor.

The schematics depicted in Figure 4 present two variations of the spike generation circuits based on the Mott memristor: one driven by a voltage source and another driven by a current source [24,25], denoted as Figures 4a and 4b respectively. To enable oscillation, the Mott memristor necessitates the presence of a capacitor (C_p). The distinctive spike waveform, with an amplitude ranging between V_{th} and V_{hold} , is generated by the charge and discharge operations of the capacitor C_p .

The frequency of the generated spikes is closely related to the C_p and connected resistor R_s in the circuits. When C_p and R_s are replaced with capacitive sensors or resistive sensors, the stimuli applied to the sensors are then encoded into the spike rates.

The spike rate f , is expressed by

$$f = \frac{1}{t_r + t_f} \quad (1)$$

where t_r and t_f are the rise time and fall time of the output voltage spikes.

As for the circuit in Figure 4a,

$$t_r = -R_H C_P \ln \left(\frac{V_{th} - V_{in} \frac{R_H}{R_S}}{V_{hold} - V_{in} \frac{R_H}{R_S}} \right) \quad (2)$$

$$t_f = -R_L C_P \ln \left(\frac{V_{hold} - V_{in} \frac{R_L}{R_S}}{V_{th} - V_{in} \frac{R_L}{R_S}} \right) \quad (3)$$

where R_H and R_L are the high resistance and low resistance of the Mott memristor.

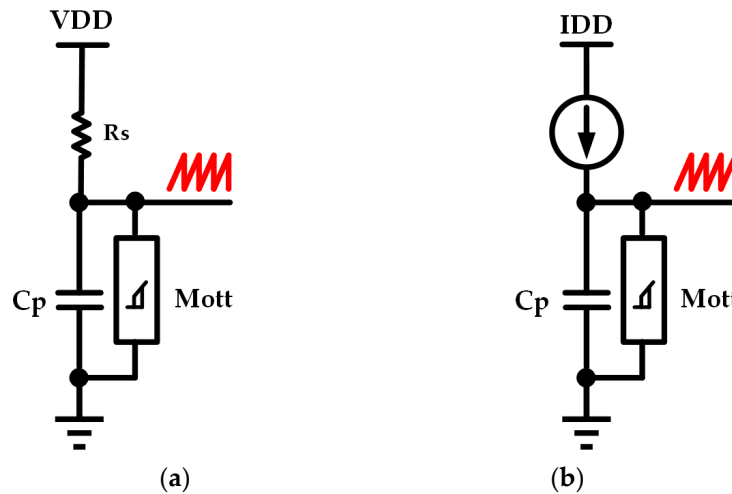


Figure 4. Schematic of the spike generation circuits based on Mott memristors: (a) driven by a voltage source and (b) driven by a current source.

As for the circuit in Figure 4b,

$$t_r = R_H C_P \ln \left(\frac{I_{in} R_H - V_{hold}}{I_{in} R_H - V_{th}} \right) \quad (4)$$

$$t_f = R_L C_P \ln \left(\frac{V_{th} - I_{in} R_L}{V_{hold} - I_{in} R_L} \right) \quad (5)$$

The recorded I-V DC sweep characteristics, together with the accompanying schematic diagrams, effectively elucidate the fundamental characteristics and operating principles of the spike generation circuit-based Mott memristor. These significant findings provide valuable insights into the behavior and functionality of the Mott memristor, thus providing a solid foundation for its potential integration and application in various electronic devices and systems.

4. Circuit and Back-End Implementation

4.1. Narrow Pulse Generator

The narrow generator circuit is shown in Figures 5 and 6. To simplify data processing, conversion of the spike wave from the Mott memristor array into a pulse wave is necessary. Initially, this is accomplished by shaping it into a square wave through the use of a comparator. The traditional scheme uses a reference voltage, as shown in Figure 5a, which means that additional voltage reference circuits are required, usually the bandgap voltage reference circuits with trimming, which apparently increases the complexity of the scheme. In addition, each Mott memristor requires a different reference voltage if the DC value of the spike wave is not fixed. Therefore, this scheme is not suitable for large sensor arrays due to inefficiency as well as inconvenience.

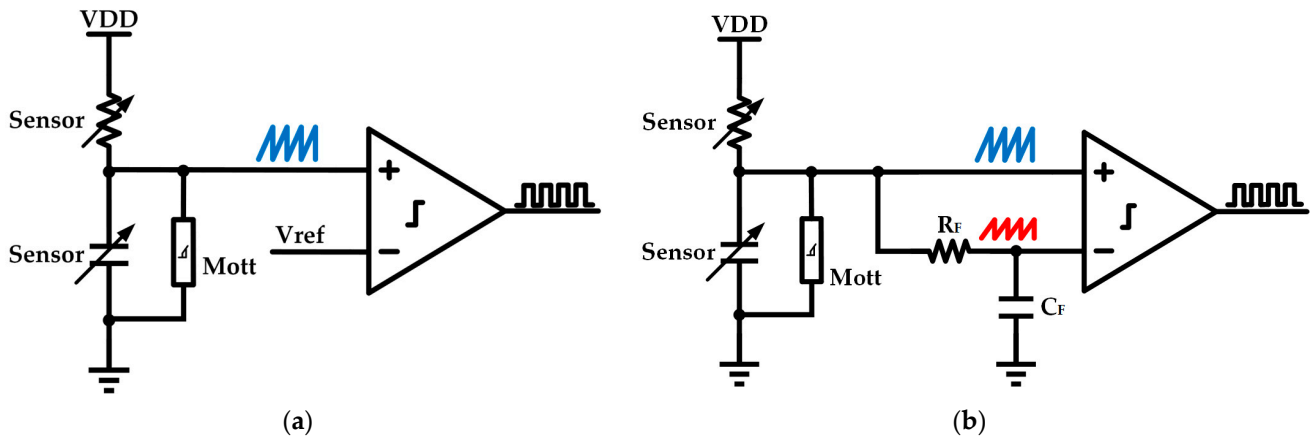


Figure 5. Spike-to-square wave conversion: (a) Comparator with reference V_{ref} . (b) Comparator with a low-pass filter.

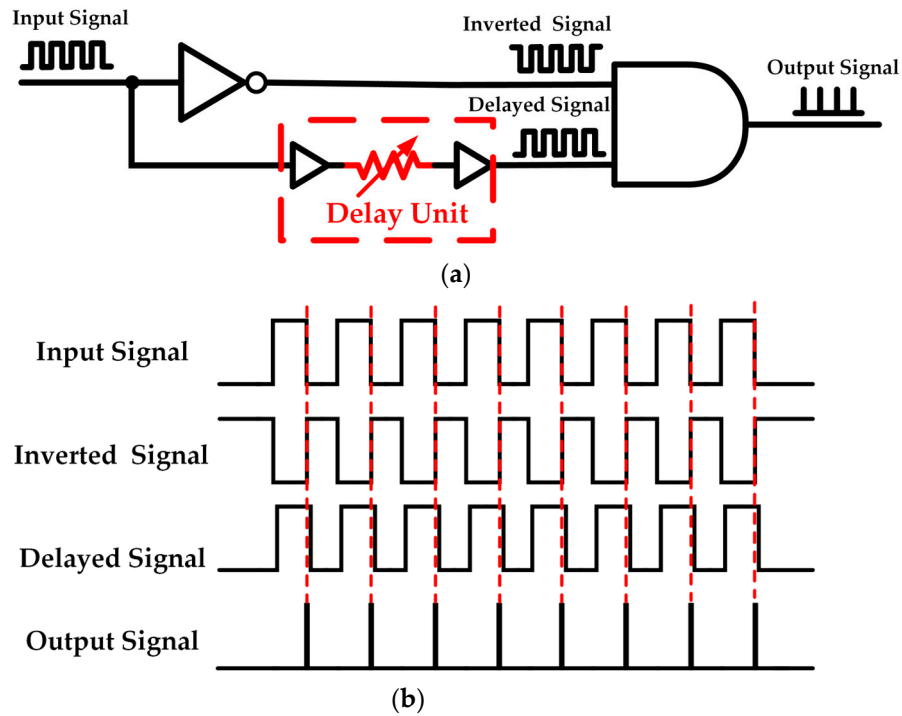


Figure 6. Square to narrow pulse wave conversion: (a) Schematic. (b) Waveform diagram.

The method used in this paper differs from the conventional approach which involves a reference voltage, as shown in Figure 5b. Instead, it involves comparing the original spike wave with the spike wave after RC low-pass filtering. This can prevent the need for varying reference voltages in the array due to the Mott memristor’s non-uniformity and DC drift.

Generating a pulse wave from a square wave requires a delay unit made up of buffers and an adjustable resistor as shown in Figure 6a [26]. And the waveform diagram is shown in Figure 6b. The square wave is split into two signals, one of which is added to an inverter and the other to the delay unit. As a result, when the square wave signal turns to “0”, the inverted signal then turns to “1” and the delayed signal briefly remains “1”, the output of the AND gate is pulled up, generating a narrow pulse at the falling edge of the square wave.

4.2. Rail-to-Rail Input Comparator

Figure 7, shows the schematic of the comparator. A rail-to-rail symmetrical amplifier is used to achieve a wide input voltage range, with transistors MN1, MN2, MP4, and MP6 forming the input stage. A buffer is also required to shape the output and improve the comparator's drive capability.

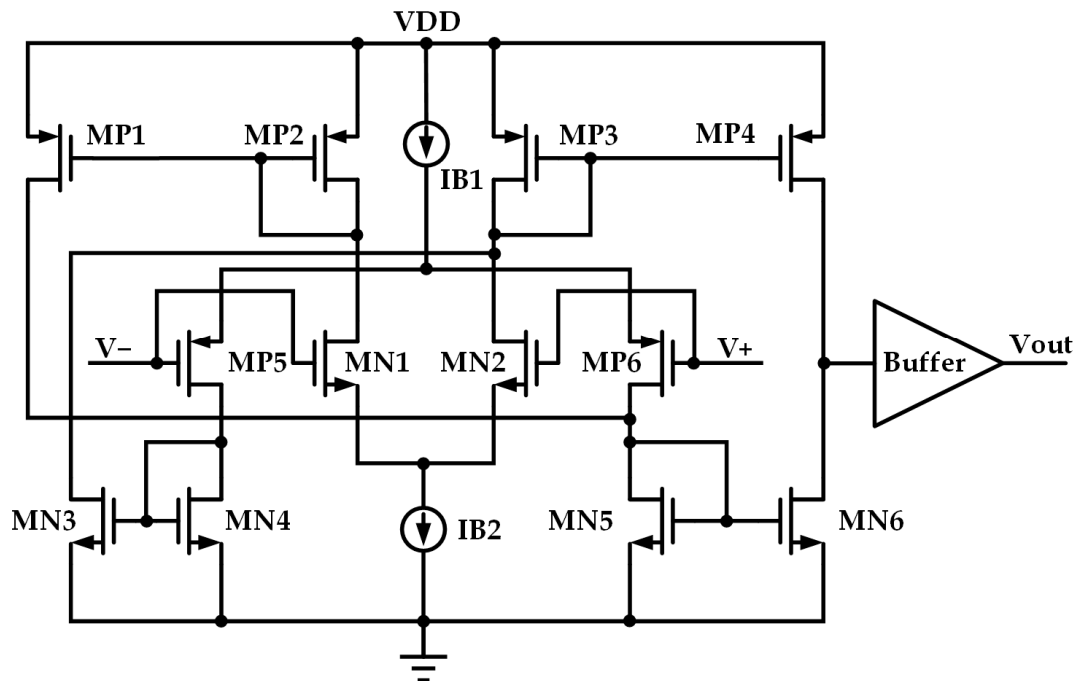


Figure 7. Schematic of designed rail-to-rail input comparator.

4.3. Greedy Strategy Data Recover

The process of the greedy search strategy for data recovery is shown in Figure 8. This operates as follows [27]: when the square wave signal that is generated by the Mott memristor passes through the multi-input OR gate for “fusion”, the pulse generation circuit transforms the different frequencies into pulse signals, significantly boosting the efficiency and success rate of the search algorithm. Subsequently, the specific positions of the rising edges of all pulses are detected and recorded in an array called $P[n]$, where n denotes the n th pulse.

Once the positions of all pulses have been recorded over a period of time, the algorithm calculates and records the distance between $P[0]$ and $P[i]$ (where $i = 1$ at the beginning of the search) as d_0 , with $P[0]$ serving as the starting point. The search then proceeds sequentially backwards, with $P[i + 1]$ as the new starting point. It determines whether there exists a $P[i + 1 + x]$ at a distance of d from $P[i + 1]$. At this juncture, two possible scenarios unfold:

- ① If such a point exists, it signals the presence of a sequence of period d between $P[0]$ and $P[n]$. The algorithm removes this sequence from the overall array and verifies whether any remaining recorded pulse positions exist. If there are remaining positions, the search algorithm continues as described above until no more recorded pulse positions remain in the array. If there are no remaining positions, the search algorithm has successfully identified the period information $d_0 \sim d_m$ represented by all the pulses in the array.
- ② If such a point does not exist, then i is incremented by 1 and the search algorithm continues as described above.

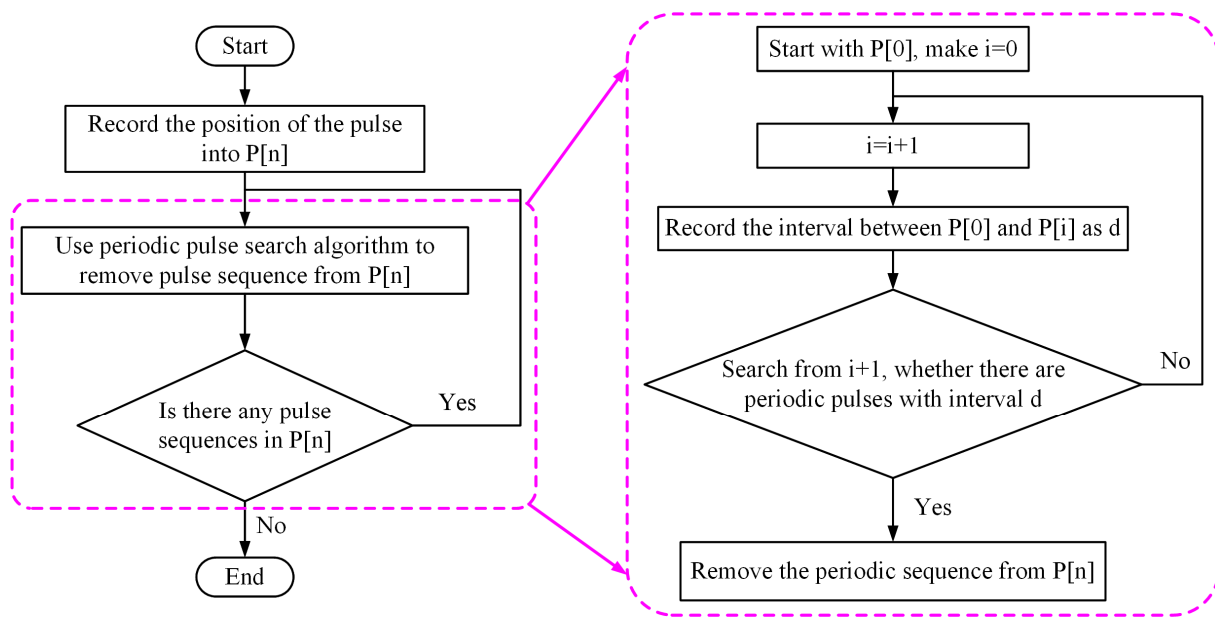


Figure 8. Process of the greedy strategy data recovery.

In summary, the greedy search algorithm leverages pulse generation circuitry to transform different frequencies of a square wave signal into pulse signals. These pulse positions are recorded in an array, and the algorithm seeks a sequence of period d between $P[0]$ and $P[n]$. If such a sequence is found, it is removed from the array and the search algorithm continues. Otherwise, the search algorithm increments i and continues searching until a sequence is found or all recorded positions have been searched.

Compared to other time–frequency conversion techniques, the greedy strategy has the advantage of being intuitive, easy to understand, and simple to implement. Once the algorithm has made a decision, there is no need to go back and check the values calculated in the previous step, eliminating the need for exhaustive operations that may be required to find the optimal solution, which apparently speeds up the time–frequency conversion considerably.

5. Experimental Results and Analysis

The innovative multi-channel sensing system proposed in this study, which leverages Mott memristor technology, demonstrates exceptional capability in efficiently processing multiple streams of sensing information through a single-signal data wire. Rigorous testing and verification procedures have been conducted to thoroughly assess the performance and reliability of the Mott memristor, the multi-channel sensing system, and the back-end greedy strategy data recovery mechanism.

Figure 9 presents an insightful visual depiction of the experimental platform utilized in the validation of the proposed sensing system. This experimental setup encompasses a 3×3 piezoresistive sensor array, a Mott memristor array, a narrow pulse generator, and an FPGA. The piezoresistive sensor array serves as the primary interface for converting external stimuli into changes in resistance, while the Mott memristor array is responsible for generating rate-coded spikes based on the detected variations. The integration of the pulse generator and FPGA facilitates the efficient processing, fusion, and transmission of the output signals from the sensor array, demonstrating the comprehensive functionality of the experimental platform.

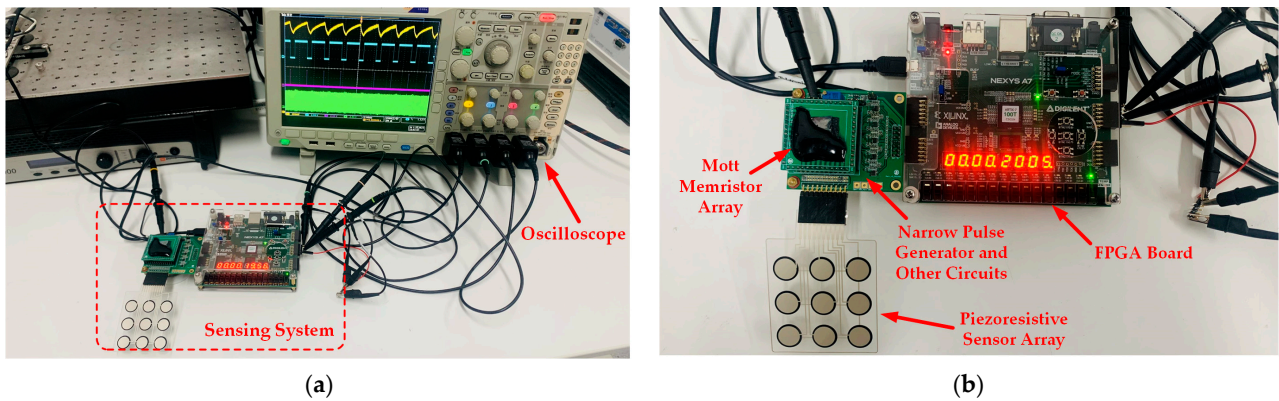


Figure 9. Photo of the experimental platform for the multi-channel sensing system, (a) test platform, (b) sensing system.

5.1. Oscillations of Mott

Figure 10 shows the oscillation driven by a voltage source. In this structure, the test conditions are an input voltage of 5 and R_S of 20 k Ω . From the oscillation data for the first 20 μ s, it can be seen that the oscillation frequency is about 1.15 MHz. In one hundred oscillation cycles, V_{th} and V_{hold} remain stable around 1.55 V and 1.20 V, respectively.

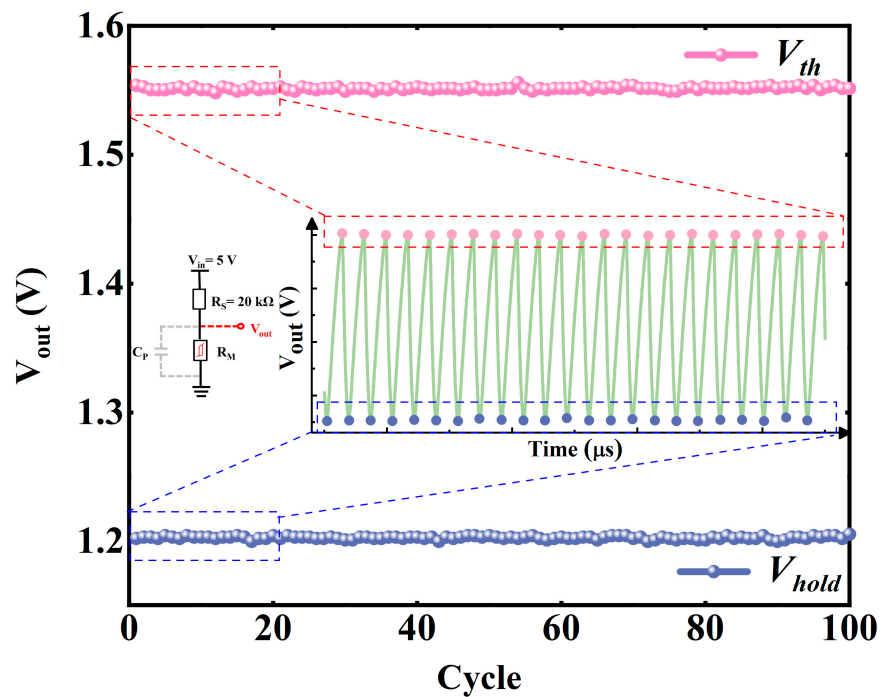


Figure 10. Oscillation driven by a voltage source, structure diagram, and the threshold voltage extracted from the oscillation diagram.

Figure 11 shows the oscillation driven by a current source. In this structure, the test conditions are an input current of 0.8 mA and C_P of 4.7 nF. From the oscillation data for the first 100 μ s, it can be seen that the oscillation frequency is about 210 kHz. In 20 oscillation cycles, V_{th} and V_{hold} remain stable around 1.55 V and 1.10 V, respectively. The measured results indicate that the Mott memristor is operating properly and stably.

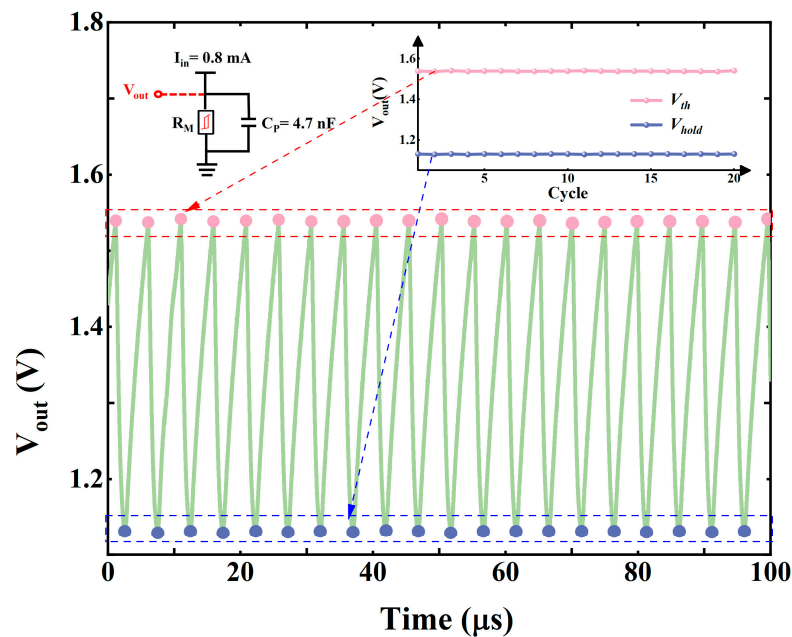


Figure 11. Oscillation driven by a current source, structure diagram, and the threshold voltage extracted from the oscillation diagram.

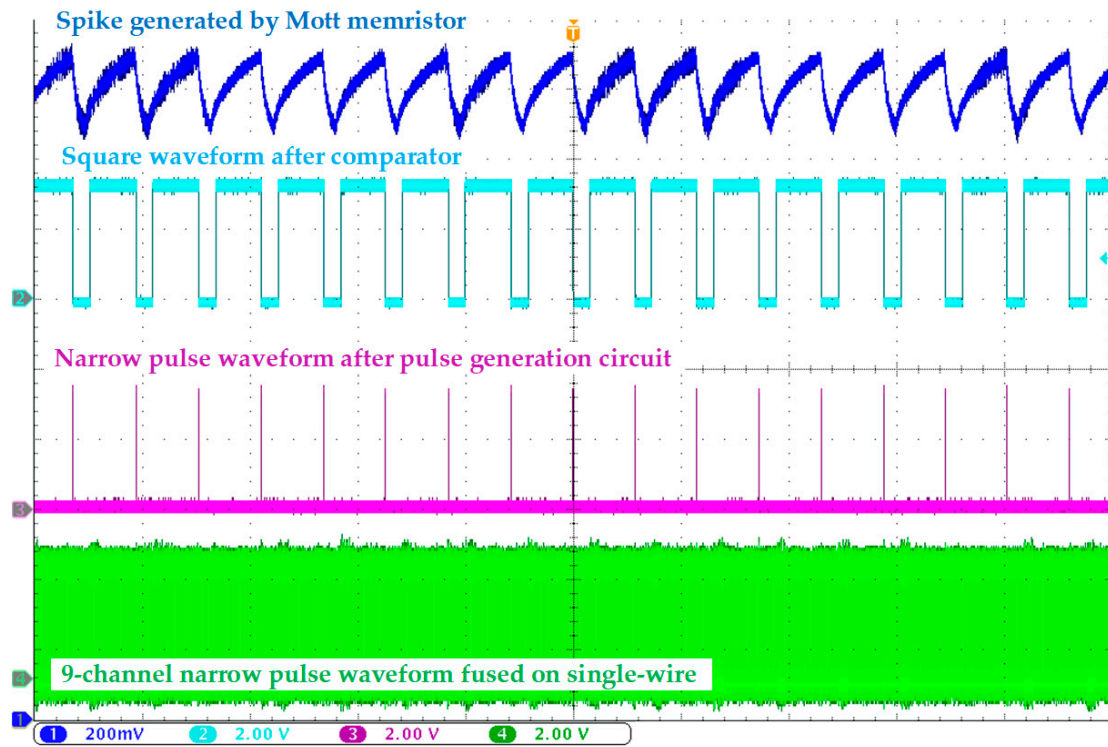
5.2. Single-Wire Output of Nine-Channel Narrow Pulse Waveforms

The Mott-based sensor interface has been measured in a previous work [11]. After several tests, the results show that at a pressure of 0.5 N, the pressure sensor resistance is 11.5 k Ω and the Mott memristor produces a stable frequency of 27.47 kHz. At pressures of 3.2 N, 4.6 N, and 8.8 N, the Mott memristor produces frequencies of 64.19 kHz, 100.10 kHz, and 137.00 kHz, respectively. In the test, the RC low-pass filter in the pulse generator has a resistance of 4.7 k Ω and a capacitance of 2.2 nF, producing a pole at 15.4 kHz. Applying different pressures to each pressure-sensitive sensor, the measured waveform of the single-wire output of the nine-channel pulse waveforms of the sensing system is shown in Figure 12a. The zoom-in waveforms and the narrow pulses with a width of 100 ns are successfully obtained as shown in Figure 12b, where the Ch-1 is the spike waveform generated by the Mott memristor, Ch-2 is the square waveform after comparator, Ch-3 is the narrow pulse waveform after the pulse generation circuit, and Ch-4 is the fused pulse waveform.

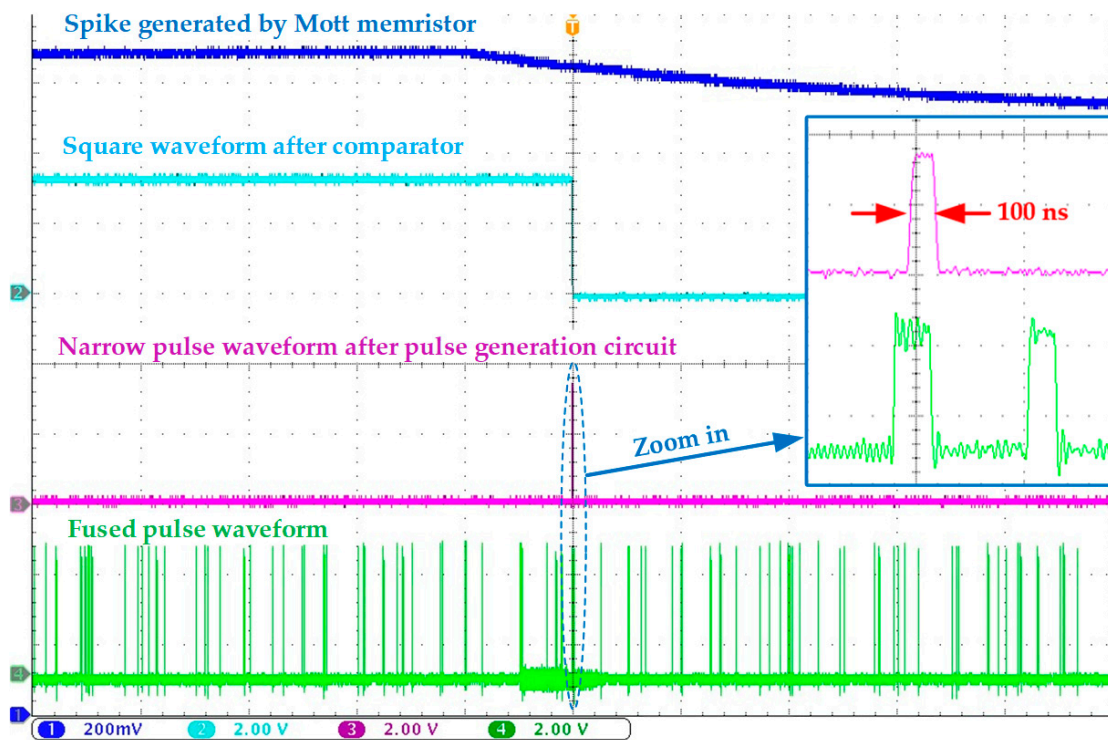
5.3. Greedy Strategy Data Recover

Considering that it is difficult to ensure constant pressures on nine piezoresistive sensors simultaneously and identify the channels, to facilitate verification of the sensing system, different R_S , C_P are set so that the Mott memristor array can generate spike waves of 10 kHz, 15 kHz, 22 kHz, 35 kHz, 50 kHz, 68 kHz, 90 kHz, 115 kHz, and 150 kHz, simulating the outputs of the piezoresistive sensor array and the Mott memristor array at different pressures. The results of greedy strategy data recovery are shown in Table 1.

The results show that data recovery using the greedy strategy is very accurate. For the actual piezoresistive sensor array, the greedy strategy is still able to recover the nine signals because the frequency of the system sampling clock is much higher than the frequency signals generated by the Mott memristors. Finally, Table 2 summarizes the performance comparison of this work with several state-of-the-art works. The proposed multi-channel sensing system utilizing Mott memristors has a wide range of applicability and can be used with various types of resistive or capacitive sensors such as light, pressure, humidity, and temperature. Multi-channel data transmission over a single wire is also an advantage for large sensor array applications.



(a)



(b)

Figure 12. Measured waveforms: (a) single-wire output of the nine-channel narrow pulse waveforms of the sensing system, (b) zoom-in waveforms.

Table 1. Results of greedy strategy data recovery.

Channel	Setting Frequency	Recovered Frequency	Error
1	10 kHz	10.005 kHz	+0.05%
2	15 kHz	15.023 kHz	+0.15%
3	22 kHz	21.952 kHz	−0.22%
4	35 kHz	35.061 kHz	+0.18%
5	50 kHz	49.751 kHz	−0.50%
6	68 kHz	67.541 kHz	−0.68%
7	90 kHz	89.597 kHz	−0.45%
8	115 kHz	115.665 kHz	+0.58%
9	150 kHz	147.783 kHz	−1.48%

Table 2. Performance summary and comparison with previously state-of-the-art sensing systems.

	JSSC-2019 [2]	ISSCC-2019 [7]	TCAS-II-2020 [9]	JSSC-2020 [15]	JSSC-2023 [28]	This Work
Syst. Architecture	SC + Zoom SAR	WhB + FIR ADC	CTC + TDC	PGA + SAR ADC	HBDC	Mott Memristor + FPGA
Process (μm)	0.18	0.18	0.065	0.18	0.18	10 (Mott Memristor Array)
Area (mm^2)	2.94	0.12	0.02	0.72	2.52	0.24
Sensor Type	Capacitive-pressure	Resistive-temperature	Capacitive unlimited	Resistive-pressure	Resistive-pressure	Resistive /Capacitive-unlimited
Channels	1	1	1	1	1	9
Data Trans. Type	--	--	Single-Wire	Single-Wire	--	Single-Wire Real-Time
Data Recover	--	--	--	--	--	Greedy strategy
Supply (V)	1.1	N/A	1	1.8	1.8	1.8–3.3
Conversion (ms)	0.85	10	0.005	1	11.52	10
Resolution	116 aF	0.16 mK	3.2 ps	--	0.24 mmHg	25 ns @ 40 MHz
Measured range	0~18.12 pF	−55–125 °C	0.82 s	--	500–1000 mmHg	Configurable
Power (W)	3.09 μ	79 μ	10 μ	12.3 μ	12.79 μ	13.0 m

6. Conclusions

In summary, we have proposed and validated a multi-channel sensing system based on Mott memristors, featuring single-wire data fusion and a back-end greedy strategy for data recovery. The key advantage of this design lies in the transmission of sensor array data through a single signal wire, and the effective data recovery achieved by the greedy strategy within an error margin of 1.5%. Leveraging Mott’s memristor enables the sensing system to achieve rapid and precise conversion at a remarkably low power consumption of only 13 mW.

Author Contributions: S.F. and P.L. proposed the architecture. S.F., S.Z. and J.X. designed the circuit and performed all of the measurements. Y.S. and C.H. wrote the initial manuscript, G.Z. supervised the manuscript. All authors have read and agreed to the published version of the manuscript.

Funding: This work was supported in part by the National Key R&D Program of China under Grant 2022YFB3203600, in part by the National Natural Science Foundation of China under Grant 62074124, and in part by the Key R&D plan of Shaanxi Province under Grant 2023-YBSF-407, 2022GY-337, and 2021GY-175.

Data Availability Statement: Data are contained within the article.

Acknowledgments: The authors would like to thank all of the editors and reviewers for their valuable comments.

Conflicts of Interest: Author Junyi Xu was employed by the company Aerial Photogrammetry and Remote Sensing Group Co., Ltd. of CNACG (ARSC). The remaining authors declare that the research was conducted in the absence of any commercial or financial relationships that could be construed as a potential conflict of interest.

References

1. Dai, G.; Du, X.; Xie, W.; Ni, T.; Han, M.; Wu, D. Circuit Design of 3- and 4-Bit Flash Analog-to-Digital Converters Based on Memristors. *Electronics* **2023**, *12*, 4069. [[CrossRef](#)]
2. Park, S.; Lee, G.-H.; Cho, S. A 2.92- μ W Capacitance-to-Digital Converter With Differential Bondwire Accelerometer, On-Chip Air Pressure, and Humidity Sensor in 0.18- μ m CMOS. *IEEE J. Solid-State Circuits* **2019**, *54*, 2845–2856. [[CrossRef](#)]
3. Huang, Y.; Li, S.; Yang, Y.; Chen, C. Progress on Memristor-Based Analog Logic Operation. *Electronics* **2023**, *12*, 2486. [[CrossRef](#)]
4. Fan, S.; Ma, W.; Lu, Z.; Han, C.; Xie, Y.; Zhang, G.; Geng, L. A Two-Step Self-Startup Hybrid Structure Step-Up Converter Using Standard 5P0 MOSFETs Achieving $36 \times$ Voltage Boosting With 50 mV Input Voltage and $84 \times$ Input Voltage Range for Self-Powered IoT Applications. *IEEE Trans. Power Electron.* **2023**, *38*, 15768–15780. [[CrossRef](#)]
5. Han, P.; Shang, J.; Pan, J.-S. A Convolution Location Method for Multi-Node Scheduling in Wireless Sensor Networks. *Electronics* **2022**, *11*, 1031. [[CrossRef](#)]
6. Zhang, C.; Gallichan, R.; Budgett, D.; McCormick, D. A capacitive pressure sensor interface ic with wireless power and data transfer. *Micromachines* **2020**, *11*, 897. [[CrossRef](#)]
7. Pan, S.; Makinwa, K.A.A. A Wheatstone Bridge Temperature Sensor with a Resolution FoM of 20fJ.K2. In Proceedings of the 2019 IEEE International Solid-State Circuits Conference (ISSCC), San Francisco, CA, USA, 17–21 February 2019; pp. 186–188.
8. Park, S.; Kim, B.; Cho, J.; Chun, J.-H.; Choi, J.; Kim, S.-J. An 80×60 Flash LiDAR Sensor with In-Pixel Histogramming TDC Based on Quaternary Search and Time-Gated Δ -Intensity Phase Detection for 45 m Detectable Range and Background Light Cancellation. In Proceedings of the 2022 IEEE International Solid-State Circuits Conference (ISSCC), San Francisco, CA, USA, 20–26 February 2022; pp. 98–100.
9. Rostami, M.S.; Saberi, M.; Maymandi-Nejad, M.; Sawan, M. A Low-Power Time-to-Digital Converter for Sensor Interface Circuits. *IEEE Trans. Circuits Syst. II* **2020**, *67*, 2853–2857. [[CrossRef](#)]
10. Zhang, C.; Gallichan, R.; Leung, D.P.; Budgett, D.M.; McCormick, D. A high-precision and low-power capacitive pressure sensor interface IC with wireless power and data transfer for a pressure sensor implant. *IEEE Sens. J.* **2023**, *23*, 7105–7114. [[CrossRef](#)]
11. Fan, S.; Lu, Z.; Ma, W. A Low-Power Sensing System Architecture With Mott Memristor and Time-to-Digital Converter for Large-Scale Sensor-Array Application. *IEEE Trans. Circuits Syst. II Express Briefs* **2023**, *10*, 3842–3846. [[CrossRef](#)]
12. Weber, M.J.; Yoshihara, Y.; Sawaby, A.; Charthad, J.; Chang, T.C.; Arbabian, A. A miniaturized single-transducer implantable pressure sensor with time-multiplexed ultrasonic data and power links. *IEEE J. Solid-State Circuits* **2018**, *53*, 1089–1101. [[CrossRef](#)]
13. Huang, P.-H.; Tu, C.-C.; Lin, T.-H. An Area-Efficient VCO-Based Hall Sensor Readout System for Autofocus Applications. In Proceedings of the 2019 IEEE International Symposium on Circuits and Systems (ISCAS), Sapporo, Japan, 26–29 May 2019; pp. 1–5.
14. Hu, H.; Gupta, S. A 0.22- μ W Single-Bit VCO-Based Time-Domain Sensor-to-Digital Front-End With Reduced Supply Sensitivity. *IEEE Trans. Circuits Syst. I* **2022**, *69*, 148–159. [[CrossRef](#)]
15. Hsu, Y.-P.; Liu, Z.; Hella, M.M. A 12.3- μ W 0.72-mm² fully integrated front-end IC for arterial pulse waveform and ExG recording. *IEEE J. Solid-State Circuits* **2020**, *55*, 2756–2770. [[CrossRef](#)]
16. Jeong, S.; Foo, Z.; Lee, Y.; Sim, J.-Y.; Blaauw, D.; Sylvester, D. A fully-integrated 71 nW CMOS temperature sensor for low power wireless sensor nodes. *IEEE J. Solid-State Circuits* **2014**, *49*, 1682–1693. [[CrossRef](#)]
17. Fan, S.; Zhao, L.; Wang, P.; Wei, R.; Zheng, X.-Q.; Wang, Z.; Feng, P.X.-L. A battery-less, 255 nA quiescent current temperature sensor with voltage regulator fully powered by harvesting ambient vibrational energy. In Proceedings of the 2017 IEEE International Symposium on Circuits and Systems (ISCAS), Baltimore, MD, USA, 28–31 May 2017; pp. 650–653.
18. Zhang, X.; Zhuo, Y.; Luo, Q.; Wu, Z.; Midya, R.; Wang, Z.; Yang, J.J. An artificial spiking afferent nerve based on Mott memristors for neurorobotics. *Nat. Commun.* **2020**, *11*, 51. [[CrossRef](#)] [[PubMed](#)]
19. Mantenuto, P.; De Marcellis, A.; Ferri, G. Uncalibrated analog bridge-based interface for wide-range resistive sensor estimation. *IEEE Sens. J.* **2012**, *12*, 1413–1414. [[CrossRef](#)]
20. Fiorillo, A.S.; Critello, C.D.; Pullano, S.A. Theory, technology and applications of piezoresistive sensors: A review. *Sens. Actuat. A Phys.* **2018**, *281*, 156–175. [[CrossRef](#)]
21. De Marcellis, A.; Ferri, G.; Mantenuto, P. Analog wheatstone bridge-based automatic interface for grounded and floating wide-range resistive sensors. *Sens. Actuators B Chem.* **2013**, *187*, 371–378. [[CrossRef](#)]
22. Gao, L.; Chen, P.-Y.; Yu, S. NbOx based oscillation neuron for neuromorphic computing. *Appl. Phys. Lett.* **2017**, *111*, 103503. [[CrossRef](#)]
23. Wang, P.; Khan, A.I.; Yu, S. Cryogenic behavior of NbO₂ based threshold switching devices as oscillation neurons. *Appl. Phys. Lett.* **2020**, *116*, 162108. [[CrossRef](#)]
24. Fang, S.L.; Han, C.Y.; Han, Z.R.; Ma, B.; Cui, Y.L.; Liu, W.; Geng, L. An artificial spiking afferent neuron system achieved by 1M1S for neuromorphic computing. *IEEE Trans. Electron Devices* **2022**, *69*, 2346–2352. [[CrossRef](#)]

25. De Marcellis, A.; Ferri, G. *Analog Circuits and Systems for Voltage Mode and Current-Mode Sensor Interfacing Applications*; Springer: New York, NY, USA, 2011.
26. Fan, S.; Wei, R.; Zhao, L.; Yang, X.; Geng, L.; Feng, P.X.-L. An Ultralow Quiescent Current Power Management System With Maximum Power Point Tracking (MPPT) for Batteryless Wireless Sensor Applications. *IEEE Trans. Power Electron.* **2018**, *33*, 7326–7337. [[CrossRef](#)]
27. Jia, Y.; Zhou, S.; Zeng, Q.; Li, C.; Chen, D.; Zhang, K.; Liu, L.; Chen, Z. The UAV Path Coverage Algorithm Based on the Greedy Strategy and Ant Colony Optimization. *Electronics* **2022**, *11*, 2667. [[CrossRef](#)]
28. Seo, D.; Cho, M.; Jeong, M.; Shin, G.; Lee, I.; Blaauw, D.; Lee, Y. An RC Delay-Based Pressure-Sensing System With Energy-Efficient Bit-Level Oversampling Techniques for Implantable IOP Monitoring Systems. *IEEE J. Solid-State Circuits* **2023**, *58*, 2745–2756. [[CrossRef](#)]

Disclaimer/Publisher’s Note: The statements, opinions and data contained in all publications are solely those of the individual author(s) and contributor(s) and not of MDPI and/or the editor(s). MDPI and/or the editor(s) disclaim responsibility for any injury to people or property resulting from any ideas, methods, instructions or products referred to in the content.